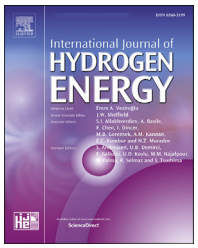
Available online at www.sciencedirect.com

ScienceDirect

journal homepage: www.elsevier.com/locate/he



Evaluating hydrogen detection performance of an electrospun $CuZnFe_2O_4$ nanofiber sensor

Ozlem Erdem Yilmaz [a,*], *Ramazan Erdem* [b]

[a] *Department of Textile Technologies, Adana Vocational School of Higher Education, Cukurova University, Adana, Turkey*

[b] *Department of Textile Technologies, Sural Vocational School of Higher Education, Akdeniz University, Antalya, Turkey*

HIGHLIGHTS

- Successful synthesis of $CuZnFe_2O_4$ nanoparticles.
- Production of neat and nanoparticle-doped nanofibers via electrospinning.
- Successful calcination process on nanofibers under various temperatures.
- Manufacturing nanofiber based hydrogen sensor.
- Investigation of hydrogen sensing performance versus various parameters.

ARTICLE INFO

Article history:
Received 26 December 2019
Received in revised form
4 June 2020
Accepted 7 June 2020
Available online 28 July 2020

Keywords:
Electrospinning
$CuZnFe_2O_4$
Nanofiber
Gas sensor
Hydrogen

ABSTRACT

$CuZnFe_2O_4$ nanoparticles (<50 nm) are successfully synthesized and incorporated in polyvinyl alcohol (PVA) to fabricate nanofibers via electrospinning technique followed by calcination process under various temperatures. Scanning electron microscopy (SEM) is used to observe the morphological characteristics of both nanoparticles and nanofibers. X-ray diffraction (XRD), Fourier transform infrared spectroscopy (FTIR) and thermo-gravimetric (TG) analyses along with energy dispersive X-ray spectrometer (EDX) analysis are conducted to evaluate structure and composition of the nanofibers, respectively. The results exhibit that the calcination temperature is substantially effective on nanofiber morphology and sensing performance in the context of forming grains (beads) on the nanofibers. The highest response and recovery performance values (response and recovery time of about 6.5 s) are obtained at the calcination temperature of 500 °C and sensor working temperature of 250 °C at 500 ppm of H2 gas concentration which also corresponds to 30% increment in detection performance compared to 300 °C-calcined nanofiber sensor. The sensor selectivity against various gases is also analyzed to compare the detection performance in air.

© 2020 Hydrogen Energy Publications LLC. Published by Elsevier Ltd. All rights reserved.

* *Corresponding author.*
E-mail address: ozlemerdem84@yahoo.com (O. Erdem Yilmaz).

https://doi.org/10.1016/j.ijhydene.2020.06.053

0360-3199/© 2020 Hydrogen Energy Publications LLC. Published by Elsevier Ltd. All rights reserved.

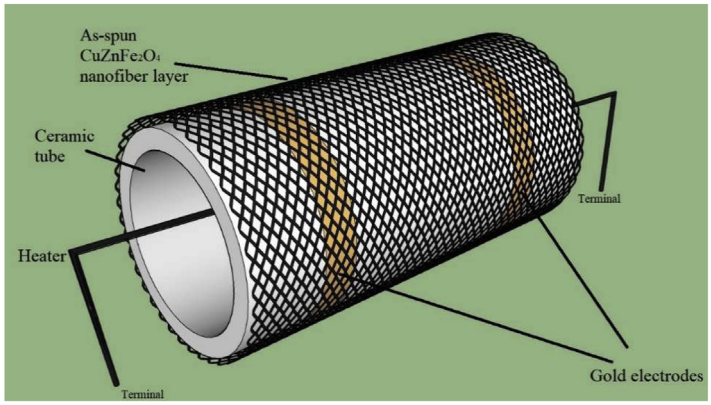
Introduction

Sensors have been utilized in variety of applications which encompass physical measures such as pressure, temperature, change in motion and impact [1–4] as well as detection of chemicals for air quality control [5,6] and healthcare monitoring [7,8]. Nevertheless, chemical sensors are of great importance in terms of sensing gases which impair the human health beginning from respiratory system in case of an exposure [9–12].

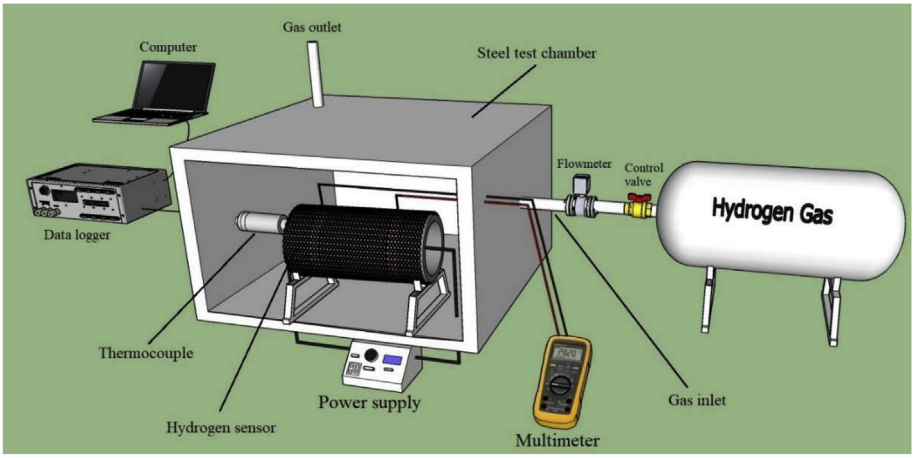
Hydrogen is an odorless, colorless, tasteless and non-toxic gas as well as being the lightest element (14.4 times lighter than air) in the nature. On the other hand, hydrogen has high deflagration potential even with low ignition energy and wide flammability range of 4–75% in air. Once combustion occurs, accelerated flame propagation leads to extreme pressure values. Thus, it has been essential to produce high precision chemical hydrogen sensors [13–18].

N-type semiconducting metal oxides have been known for their good gas sensing [19], optical and electronic properties as well as providing wide usage in solar cells, environmental and biological fields [20–23]. Recently, conductometric sensors comprising metal oxide nano-belts have been attaining reputation due to their large surface/volume ratio providing notable current changes towards various gases [17,19,24]. In this context, many studies have been conducted on gas detection sensitivity against target gases [10–12,17]. Among them, nano-crystalline zinc ferrite comes into prominence in terms of gas sensing thanks to its thermal and chemical stability, good selectivity and large specific area [12,25–28]. Though there have been several methods to produce zinc ferrite structures such as facile co-precipitation [29–31] and sol-gel [32–34], electrospinning steps forward as an appropriate method to prepare three-dimensional (3-D) nanostructures easily from organic-inorganic materials due to its high productivity, simplicity, versatility and cost-effectiveness [12,35,36]. As gas sensing is related to change in surface conductivity when exposed to a gas, thin film production process such as electrospinning steps forward [37–39]. On the other hand, there are peculiar materials that can be used as sensing substrate. Among these Pd-based materials require lower energy consumption for sensor heating while being vulnerable to impurity in air (poisoning) [40].

Besides zinc ferrite, many sensors consisting of copper-based material such as copper (II) oxide (CuO) have been appealing to researchers [41–43]. Yet, hydrogen-sensing properties of copper-based zinc ferrite sensors have remained unreported. Thus, investigation of hydrogen-sensing performance of a metal oxide compound ($CuZnFe_2O_4$) comprised of semiconductor n-type components with high hydrogen-sensing efficacy is required to fill the gap in the literature. In this context, this study aims to manufacture a

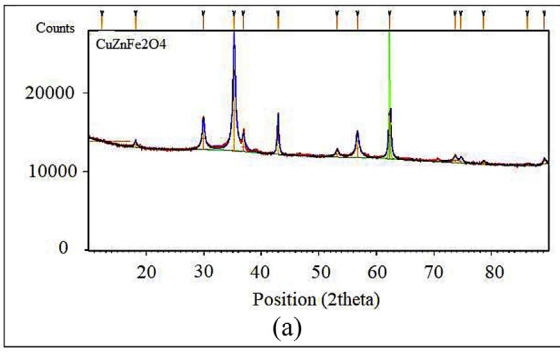


(a)



(b)

Fig. 1 – Illustration of the (a) H_2 sensor, (b) test bench.



Pos. [°2θ]	Lattice Planes	Crystallite Size [Å]	Crystallite Diameter [nm]
18.1672	111	126	12.6
29.9385	220	112	11.2
35.2640	311	128	12.8
36.8727	222	89	8.9
42.8966	400	287	28.7
53.1843	422	80	8.0
56.7101	511	100	10.0
62.2999	440	232	23.2
73.6614	533	50	5.0
74.7074	444	488	48.8
78.6256	642	109	10.9
86.2372	731	23	2.3
89.1607	744	437	43.7

(b)

Fig. 2 – XRD results of the synthesized nanoparticles, (a) XRD patterns, (b) structural data.

hydrogen sensor based on electrospun $CuZnFe_2O_4$ nanofibers with high hydrogen sensitivity, good response-recovery time and high selectivity.

Experimentation

Synthesis of $CuZnFe_2O_4$ nanoparticles

Three metal salts [$Cu(NO_3)_2 \cdot 6H_2O$, $Zn(NO_3)_2 \cdot 6H_2O$, $Fe(NO_3)_3 \cdot 9H_2O$] were purchased from Merck Co. and polymer solution (PVA, Mw ≈ 125,000) was supplied from Sigma Aldrich. All chemicals were of analytical grade and used without any further treatment.

The metal salts in stoichiometric amounts (Cu, Zn and Fe nitrates) were dissolved in deionized water prior to addition of oxalic acid (1:1 M ratio) to the obtained aqueous solution of the metal nitrates. The mixture solution underwent rigorous stirring process for 2 h at room temperature using a magnetic stirrer. After evaporating the resultant mixtures, the obtained brown powder was dried in oven at 200 °C for 24 h [44].

Electrospinning process

Two different electrospinning solutions (undoped PVA and PVA+0.12 g $CuZnFe_2O_4$) were firstly prepared. PVA (6 wt%) was dissolved in distilled water and kept in autoclave at 120 °C for 20 min to obtain homogenous solution. In order to prepare mixed solutions, various amount of $CuZnFe_2O_4$ compound was introduced in the PVA solution and stirred for 6 h at room temperature. The amount of $CuZnFe_2O_4$ compound in the solution had to be no more than 0.12 g to avoid electrolytic solution which impairs a fluent electrospinning process.

A laboratory type electrospinning set-up with high voltage power supply for generating electromagnetic field (Matsusada Handy Type) and microfluidics syringe pump for solution feeding (as prepared polymer solutions) (NE 1002X) were used to obtain nanofibers (electrospun fibers).

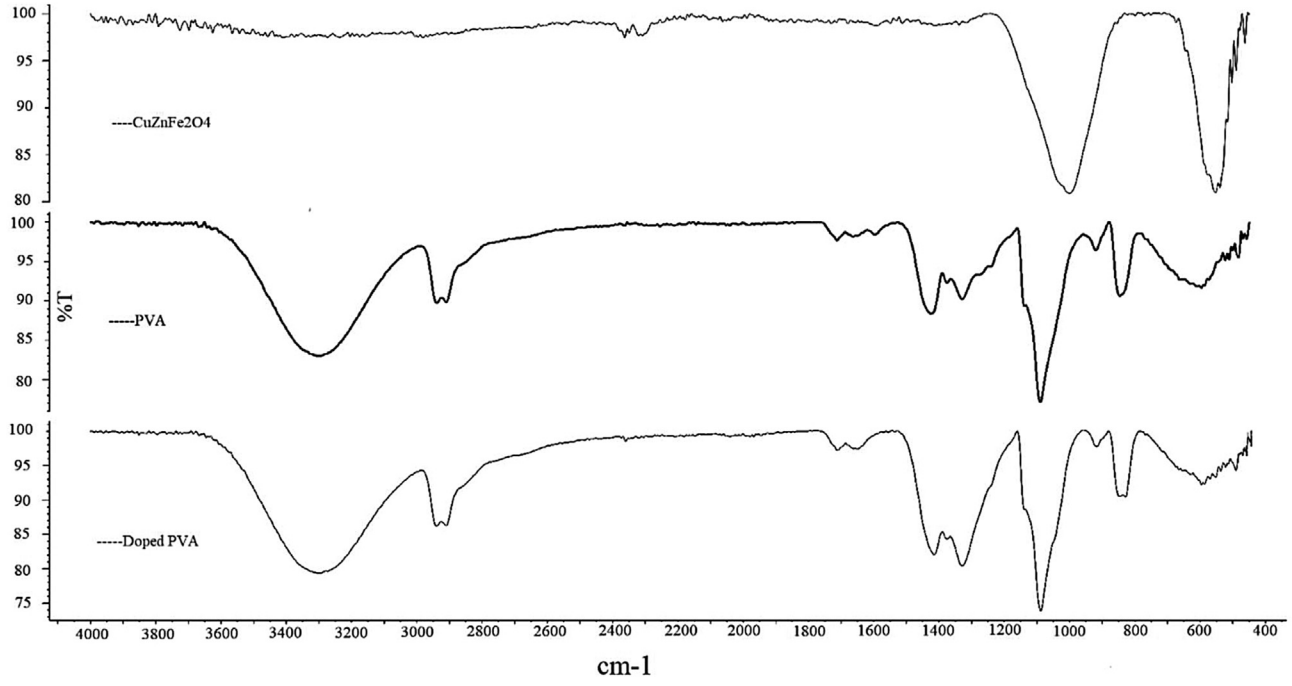
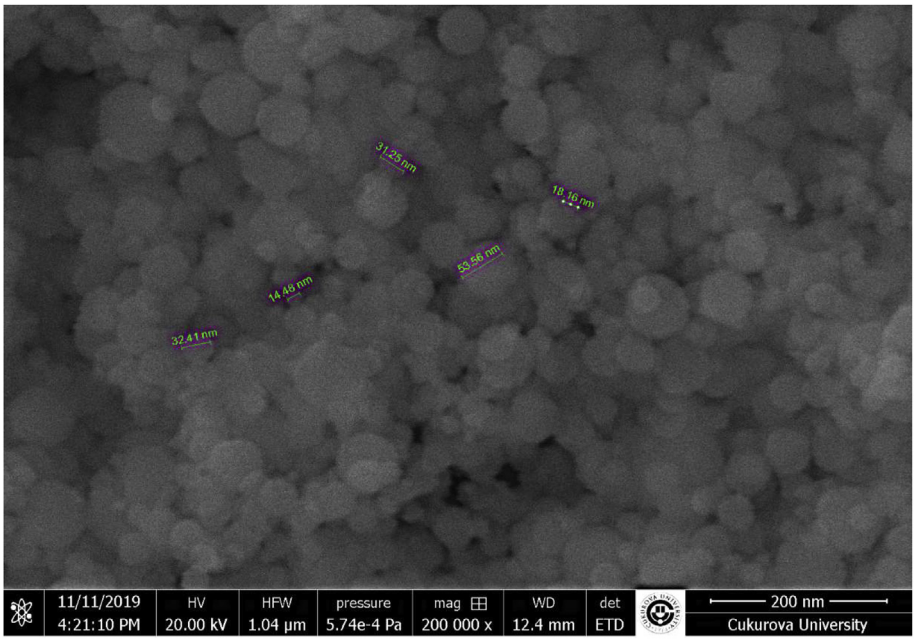
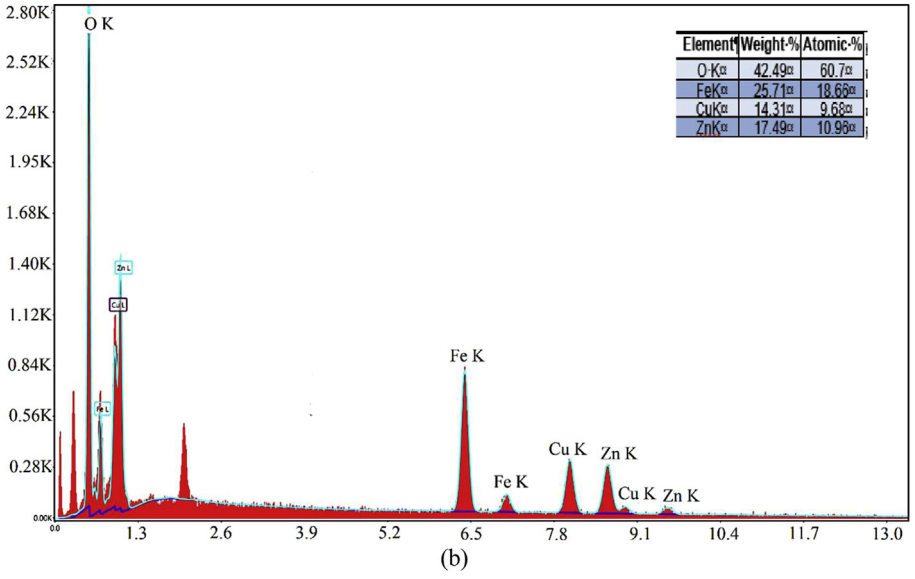


Fig. 3 – FTIR spectra of $CuZnFe_2O_4$ nanoparticles, undoped and doped PVA.



(a)



(b)

Fig. 4 – (a) SEM images and (b) chemical composition of the nanoparticles.

4 mL syringe with 20-gauge nozzle was utilized to inject each solution towards the collector (a drum covered with aluminum foil and 24 cm away from the nozzle) through a potential difference of +22.5 kV (AC). The syringe pump was adjusted to send each solution to the drum horizontally at a flow rate of 0.05 mL/h. The experiments were conducted at 40–42% RH and 28–31 °C.

Characterization of the nanoparticles and electrospun fibers

The structural characterization of the synthesized nanoparticle was performed by SEM (Quanta 650) analysis to define the particle size and morphology. FTIR (Jasco-6700) spectra of the products was determined to observe structural behavior. X-ray (Panalytical Empyrean) diffraction patterns (XRD) were also analyzed to have comprehensive knowledge about the structure. The thermal stability of the nanoparticles was examined via TG (Mettler Toledo). Nanograin size of nanofibers was calculated utilizing Scherrer formula. Electrospun fibers were morphologically analyzed via SEM images obtained at a magnification of 200000x. Elemental analysis was performed by EDX coupled with the SEM device.

Sensor preparation and the test rig

Electrode printed ceramic tubes (with Pt heating wire) were covered separately with the as-spun fibers calcined at temperatures ranging from 300 to 600 °C in a high-temperature furnace (in air) to remove most of the organic components and enhance crystallinity. Subsequent to reaching stable

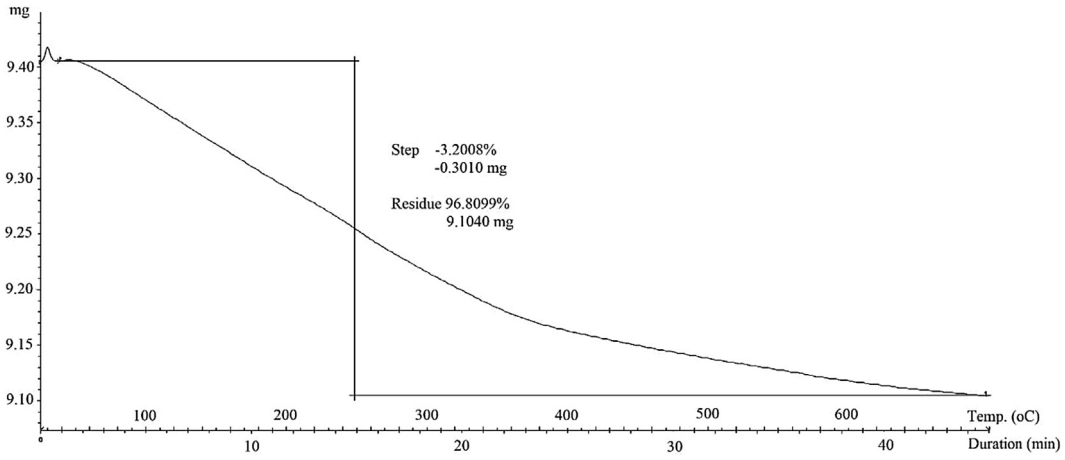


Fig. 5 – Thermal stability characteristics of the synthesized nanoparticles.

resistance in air, each sensor was placed in a well-sealed steel chamber in which the hydrogen gas (99.99% purity) was introduced through an isolated control valve and high precision flow meter. Upon exposure of H_2 gas, the resistance (R_g) and sensor operation temperature data were collected via a multimeter and temperature sensor, respectively to an extent in which the stable resistance level was reached (response). After H_2 sensing tests, sensors were exposed to air until 90% change in resistance (R_a) was reached (recovery) [17,45]. Fig. 1(a) and (b) illustrate the as-prepared sensor and test bench used in this work, respectively.

Results and Discussion

Characterization of the synthesized nanoparticles

X-ray diffraction patterns of the synthesized $CuZnFe_2O_4$ nanoparticles (Fig. 2) clearly depict high single crystallinity with (220), (311), (400), (422), (511) and (440) major lattice planes. Specifically, intense peak at (311) indicates the spinel cubic structure of the Fd-3m space group which is consistent with the powder diffraction file of JCPDS [46].

Peak distribution list given in Fig. 2(b) points that the synthesis product is in crystal structure with low diameter. Average crystal diameter is found considering full-width at half-maxima (FWHM) where peak positions are computed via Scherrer's equation [$D = k\lambda/(\beta \cos\theta)$] [47]. Calculations show that the crystal has a spherical geometry with diameter of between 5 and 50 nm which can also be seen in SEM images (Fig. 4(a)).

Characteristic peaks of the metals are generally observed within the fingerprint region. According to FTIR spectrum of synthesized nanoparticles, peaks at 417 cm^{-1} and 550 cm^{-1} indicate the existence of Zn–O and Fe–O [48]. For CuO, prominent peaks are likely to be seen at broad bands of 525 cm^{-1}, 580 cm^{-1} and 675 cm^{-1} [49]. As seen in FTIR spectrum of neat PVA and doped-PVA (Fig. 3), the characteristic broad band at 3401 cm^{-1} and 2919 cm^{-1} are attributed to the O–H and C–H stretching vibrations, respectively. The bending vibration of O–H observed at 1435 cm^{-1}. The peak at 1096 cm^{-1} is due to the C–O stretching band of secondary alcohol [50,51].

The morphology of synthesized nanoparticles is examined via detailed SEM images. SEM images demonstrate that synthesized nanoparticles have spherical shape with average diameter of below 50 nm (Fig. 4(a)). Referring to EDX spectra; Cu, Zn, Fe and O are in expected atomic ratios (1:1:2:4) which are compatible with $CuZnFe_2O_4$ chemical formula. The only presence of Cu, Zn, Fe and O clearly indicates the high purity of the synthesized compound.

Thermal stability (TG) analysis is of great importance to observe structural behavior of the nanoparticles when calcined at relatively high temperatures [52]. Fig. 5 plots the weight loss with respect to various temperature values. A weight loss of about 3.2% was determined in the range of

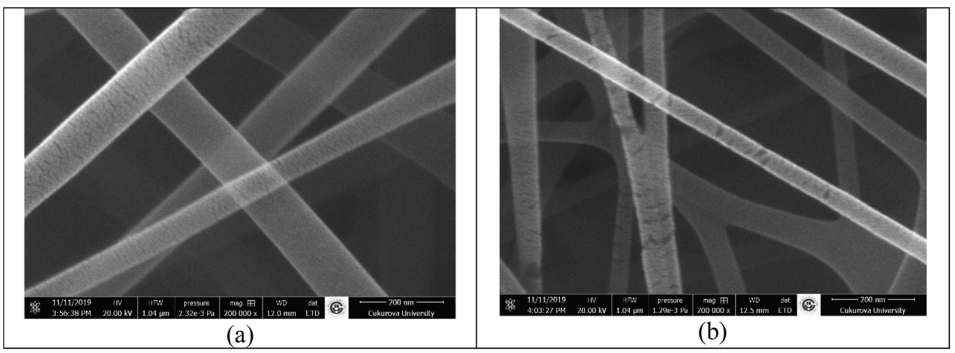


Fig. 6 – SEM images (200 nm) of as-spun fibers before calcination process; (a) undoped PVA, (b) $CuZnFe_2O_4$-doped PVA.

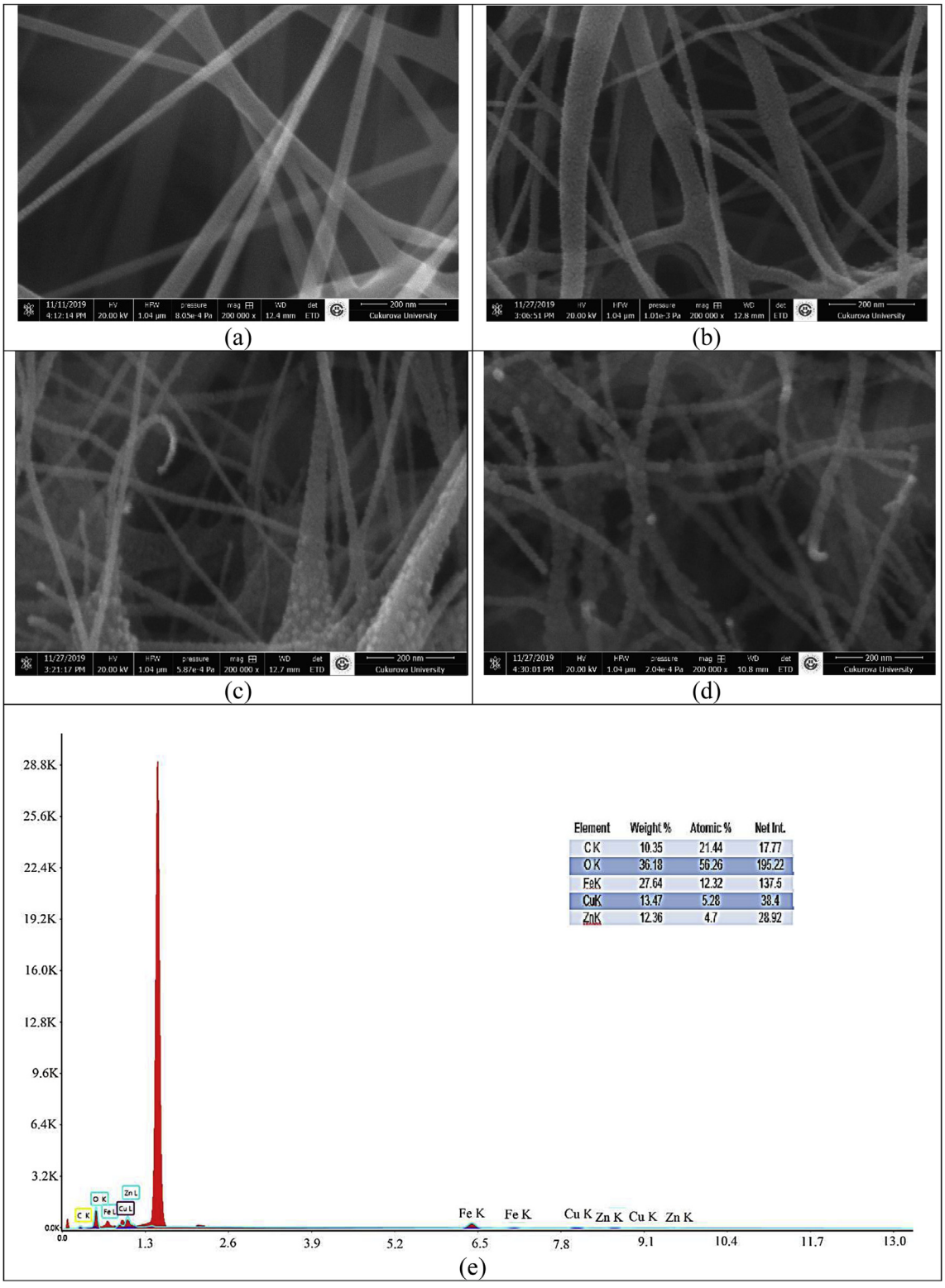


Fig. 7 – SEM images (200 nm) of the doped fibers calcined at: (a) 300 °C, (b) 400 °C, (c) 500 °C, (d) 600 °C and (e) EDX spectra of the doped fibers calcined at 500 °C.

30–700 °C due to evaporation of residual water in hollows of the spheres within the $CuZnFe_2O_4$ nanostructure. The carbon was completely combusted at a relatively low temperature (<400 °C). TG results present that the electrospun fibers doped with synthesized nanoparticles are likely to undergo calcination process at elevated temperatures due to their capability of maintaining their stability.

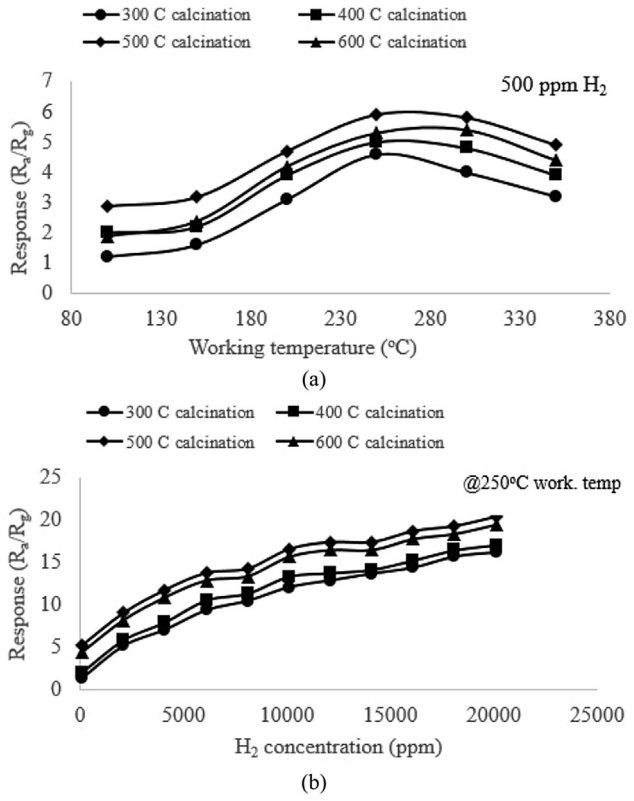


Fig. 8 – Response vs. (a) working temperature, (b) H_2 concentration.

Morphological and structural characteristics of electrospun nanofibers

Fig. 6(a) and (b) exhibit the SEM images of the fibrous electrospun membrane structures, resembling spider nets with uniform and well-dispersed fibers consist of neat (undoped) PVA and $CuZnFe_2O_4$-doped PVA before the calcination process. Average fiber diameter for neat PVA was found to be about 112 ± 22 nm whereas it was 54 ± 14 nm for $CuZnFe_2O_4$ incorporated fibers. This decline in the fiber diameter can be explained with the increased solution conductivity. As the amount of metal compound increases in the system, solution becomes more ionic which leads to higher electrostatic forces exerted on the polymer jet during electrospinning. Consequently, a significant increment in whipping instability level occurs and thinner fibers are obtained [53].

Fig. 7 illustrates the morphological structure of $CuZnFe_2O_4$-doped as-spun fibers annealed at the temperature range of 300–600 °C along with the chemical composition of the fibers annealed at 500 °C. Fibers extracted from undoped PVA were prone to melt down at the calcination temperature range used in this study. Thus, only SEM images of the fibers produced using doped PVA solutions were given and interpreted. It was noticed that $CuZnFe_2O_4$-doped electrospun fibers acquired smooth surface and were shrunk to lower average diameter of 34 ± 4 nm when annealed at 300 °C. Nevertheless, when the calcination temperature was increased to 400 °C, the fiber diameters slightly diminished (24 ± 10 nm) and some beading formation was observed on the fibers due to the $CuZnFe_2O_4$ content and decomposition of the polymer during calcinations [12]. Furthermore, beads formed on the fibers became more distinctive and the fiber diameters were calculated as 18 ± 9 nm in average at the annealing temperature of 500 °C.

Sensing performance

As gas sensing mechanism, before hydrogen exposure, ambient oxygen molecules are adsorbed and the surface loses electron. This chemisorption process provides new oxygen species (O, O^-, O^{2-}) as shown in Eqs. (1)–(3). Electron loss on the metal oxide (Mox) surface leads to reduced concentration through the conduction band and increased initial resistance [54].

$$O_2\ (gas) \rightarrow 2O\ (adsorbed) \quad (1)$$

$$O\ (adsorbed) + e^-(from\ Mox) \rightarrow O^- \quad (2)$$

$$O\ (adsorbed) + 2e^-(from\ Mox) \rightarrow O^{2-} \quad (3)$$

Upon exposure to hydrogen gas, hydrogen molecules are converted into atoms and adsorbed to the surface due to catalytic effect (spillover effect). Hydrogen atoms react with pre-adsorbed oxygen ions in which the water vapor was formed as product and electrons are released (Eq. (4), (5) and (6)). Reduction of electron concentration on the surface provides reduction in resistance and improvement in conduction which is a typical specification of the n-type semiconductors [55].

$$H_2 \rightarrow 2H\ (adsorbed) \quad (4)$$

$$2H\ (adsorbed) + O^- \rightarrow H_2O + e^- \quad (5)$$

$$2H\ (adsorbed) + O^{2-} \rightarrow H_2O + 2e^- \quad (6)$$

The effect of working temperature of the sensor comes into prominence in the context of sensing performance and needs to be analyzed to achieve optimal temperature value [17,56]. Fig. 8(a) depicts the response performance of the sensor as-wrapped with nanofibers calcined at various temperatures for 500 ppm of H_2 gas concentration. When the sensor is

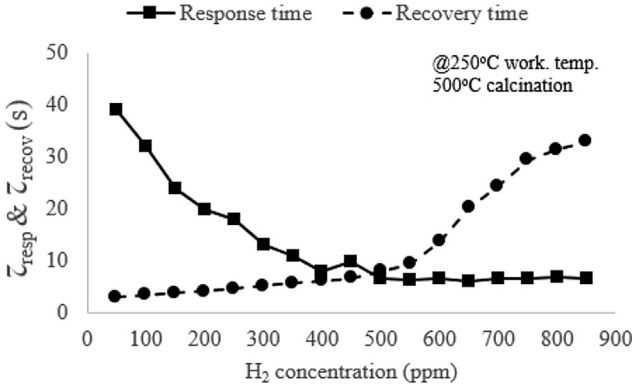


Fig. 9 – Response and recovery time vs. H_2 concentration.

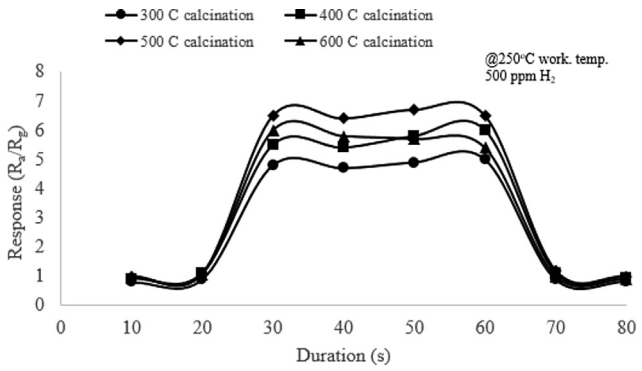


Fig. 10 – Response to 500 ppm of H_2 at 250 °C working temperature vs. test duration.

exposed to the target gas after recovery in air, the resistance during the H_2 gas exposure (R_g) tends to decrease until about 250 °C of sensor operating temperature which leads to improved response performance (higher R_a/R_g) for all sensors comprised of nanofibers calcined at different temperatures. The sensing performance is substantially influenced by the grain (bead) size and crystallinity of the nanofibers of which are deemed as a function of calcination temperature [57,58]. The response reaches its maximum at about 5.9 under 250 °C of working temperature for as-prepared sensors wrapped with nanofibers annealed at 500 °C. Thus, in subsequent sections of the study, 250 °C was selected as the sensor operating temperature during analyses. This may be attributed to enhancement of reaction rate occurring during the H_2 gas flow over the nanofiber layer due to temperature increment. On the contrary, the adsorbed gas tends to flee from the layer before the recurrent reaction when the operating temperature is too high resulting in diminished response [59–61].

The response as a function of H_2 gas concentration for all sensors with nanofibers annealed at four different temperatures and at sensor operating temperature of 250 °C is shown in Fig. 8(b). In general, the response depicted an increasing trend (as of 100 ppm) as the gas concentration soared and reached a stable value above concentration of 20,000 ppm showing that no more H_2 gas reacts with the sensor due to getting saturated. The response obtained for sensor with 500°C-calcined nanofibers is improved as much as approximately 30% compared to that of the sensor with 300°C-calcined nanofibers.

Fig. 9 plots the variation of response ($+_{resp}$) and recovery ($+_{recov}$) time with respect to H_2 gas concentration in the gas concentration range of 50–850 ppm. The best response and recovery time of around 6.5 s was achieved at about 500 ppm which is explained as the improvement of active sites due to placement of nanofiber layer on the substrate (sensor). Exposure to the reducing gas (H_2) induces resistance reduction, which is a typical feature of n-type semiconductors [61,62] and alters the response performance. Conversely, insufficient amount of H_2 gas causes limited diffusion into the surface resulting in poor response time for low gas concentrations [63]. As expected, concentration increment leads to requirement of more time for sensor to recover.

During H_2 sensing process, the sensor is expected to approach to saturation resulting in reduced response performance even under constant gas flowrate and operating temperature. Fig. 10 shows the response characteristics of the sensor covered with various nanofibers annealed at different temperatures with respect to test duration over 75 s. The results related to each test (500 ppm of H_2, 250 °C work. Temp., repeated in triplicate and averaged to minimize data scattering) present that the sensor used in each trial was prone to exhibit maximum response performance between 30th and 65th seconds. This can be explained with the increasing reaction rate, to an extent, taking place between the sensor nanofiber layer and the H_2 gas. When the H_2 gas is introduced into the test chamber, the redox reactions commence,

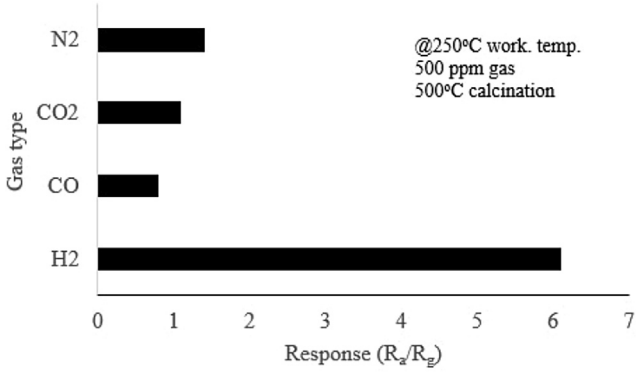


Fig. 11 – Response of the sensor with 500°C-calcined nanofiber to 500 ppm of H_2, CO, CO_2 and N_2 at 250 °C working temperature.

Table 1 – Comparison of hydrogen sensing performance of various metal oxides [64,65].

Sensor base material	Sensor working temp. (°C)	Detection range	Sensing parameter	Active surface type	Response time (s)
$CuZnFe_2O_4$-doped nanofiber	250	50-850 ppm	Electrical resistance	Paste onto ceramic tube with gold electrodes	~6.5
Al_2O_3, Bi_2O_3 [66]	450	9%	Electrical resistance	Thin film	<60
SnO_2 [67]	25–575	50–1000 ppm	Electrical resistance	Wrapped Pt wire coil	12–25
SnO_2–Pd [68]	200–450	0.5 vol%	Electrical resistance	Film	5–7
Fe_2O_3 [69]	320	500–2000	Electrical resistance	Thin film	4
TiO_2 nanotube [70]	25–250	1000	Electrical resistance	Thin film	30
3 wt% ZnO–SnO_2 in CuO [69]	305	200	Electrical resistance	Pellet	16
SnO_2 in 2.6 mol% ZnO [71]	350	100	Electrical resistance	Nanorod	18.4

develop, reach their maximum and sustain for a period until the surface comes to saturation.

As mentioned in the manuscript, there are directly effective parameters on sensing performance such as sensor base material, working temperature, active surface type and hydrogen flow rate. Thus, a comparison amid response time of various metal oxides is likely to be made as shown in Table 1.

For a H_2 sensor design, it would not be prudent unless the sensor does not exhibit the similar sensing performance towards gases apart from H_2, i.e. for a hydrogen detector. In other words, the sensor is likely to be selective for the target gas in air. To determine selectivity, the sensor was also exposed to CO, CO_2 and N_2 gases which are abundantly found in air. Fig. 11 demonstrates the sensing performance of the sensor upon exposure to various gases and response to H_2 gas was the most pronounced of all, indicating that the sensor has high H_2 selectivity.

Conclusion

A high response hydrogen sensor wrapped with nanofibers calcined at four different temperatures was successfully manufactured. The results depict that the sensing performance strongly depends on annealing temperature, hydrogen gas concentration and sensor working temperature. The maximum response of 6.5 was achieved for the as-prepared sensor; covered with nanofibers annealed at 500 °C, operating at 250 °C for 500 ppm of H_2. This high response can be attributed to optimal parameters which enhance reaction efficacy. On the other hand, the sensor reaches saturation over a specific gas concentration and the response tends to decrease due to depletion of active sites on the surface. It is believed that this study will be a guide in the context of safe hydrogen usage, storage and/or transportation.

Funding

This study was financially supported by Cukurova University, Department of Scientific Research Projects with Grant number: 12,524.

Declaration of competing interest

The authors declare that they have no known competing financial interests or personal relationships that could have appeared to influence the work reported in this paper.

Acknowledgment

The authors would like to thank Chemistry Laboratories of Cukurova University and Akdeniz University for giving opportunity to conduct this experimental study.

REFERENCES

[1] Rohrmann K, Sandner M, Meier P, Prochaska M. A novel readout technique for magnetoresistive sensors in automotive anti-lock braking systems. In: Proc IEEE Int Symp Circ Syst; 2018. p. 1–5. 2018-May.
[2] Kim YK, Kang H, Kim JK. Directly attached airbag sensor packaging for automobiles. In: 2016 Pan Pacific Microelectron Symp Pan Pacific; 2016. p. 1–3.
[3] Tian H, Shu Y, Wang XF, Mohammad MA, Bie Z, Xie QY, et al. A graphene-based resistive pressure sensor with record-high sensitivity in a wide pressure range. Sci Rep 2015;5:1–6.
[4] Nguyen LV, Warren-Smith SC, Ebendorff-Heidepriem H, Monro TM. Interferometric high temperature sensor using suspended-core optical fibers. Optic Express 2016;24:8967.
[5] Zhou J, Li P, Zhang S, Long Y, Zhou F, Huang Y, et al. Zeolite-modified microcantilever gas sensor for indoor air quality control. Sensor Actuator B 2003;94:337–42.
[6] Kim YS, Hwang IS, Kim SJ, Lee CY, Lee JH. CuO nanowire gas sensors for air quality control in automotive cabin. Sensor Actuator B 2008;135:298–303.
[7] Lorwongtragool P, Sowade E, Watthanawisuth N, Baumann RR, Kerdcharoen T. A novel wearable electronic nose for healthcare based on flexible printed chemical sensor array. Sensors 2014;14:19700–12.
[8] Kim J, Campbell AS, de Ávila BEF, Wang J. Wearable biosensors for healthcare monitoring. Nat Biotechnol 2019;37:389–406.
[9] Seo Y, Memon MU, Lim S. Microfluidic eighth-mode substrate-integrated-waveguide antenna for compact ethanol chemical sensor application. IEEE Trans Antenn Propag 2016;64:3218–22.
[10] Aslani A, Oroojpour V. CO gas sensing of CuO nanostructures, synthesized by an assisted solvothermal wet chemical route. Phys B Condens Matter 2011;406:144–9.
[11] Nagarajan V, Chandiramouli R. Detection of trace level of hazardous phosgene gas on antimonene nanotube based on first-principles method. J Mol Graph Model 2019;88:32–40.
[12] Van Hoang N, Hung CM, Hoa ND, Van Duy N, Van Hieu N. Facile on-chip electrospinning of $ZnFe_2O_4$ nanofiber sensors with excellent sensing performance to H_2S down ppb level. J Hazard Mater 2018;360:6–16.
[13] Cutrono Rakhimov A, Visser DC, Holler T, Komen EMJ. The role of CFD combustion modelling in hydrogen safety management–VI: validation for slow deflagration in homogeneous hydrogen-air-steam experiments. Nucl Eng Des 2017;311:142–55.
[14] Goulier J, Chaumeix N, Halter F, Meynet N, Bentaïb A. Experimental study of laminar and turbulent flame speed of a spherical flame in a fan-stirred closed vessel for hydrogen safety application. Nucl Eng Des 2017;312:214–27.
[15] Karaduman I, Barin O, Yildiz DE, Acar S. Atomik tabaka biriktirme metodu ile uretilen HfO_2 tabanli sensörlerin hidrojen gaz algilama özelliklerinin incelenmesi/ Investigation of hydrogen gas sensing properties of HfO_2 based sensor produced by atomic layer deposition method. J Polytech 2016;19:223–9.
[16] Prezhdo VV, Vashchenko EV, Prezhdo OV, Pushko A. Structure and properties of hydrogen bonded complexes of pyridine-N-oxide and its derivatives. J Mol Struct 1999;510:69–83.

[17] Xu X, Sun J, Zhang H, Wang Z, Dong B, Jiang T, et al. Effects of Al doping on SnO_2 nanofibers in hydrogen sensor. Sensor Actuator B 2011;160:858–63.
[18] Hung CW, Lin HL, Chen HI, Tsai YY, Lai PH, Fu SI, et al. Comprehensive study of a Pd-GaAs high electron mobility transistor (HEMT)-based hydrogen sensor. Sensor Actuator B 2007;122:81–8.
[19] Huang J, Wan Q. Gas sensors based on semiconducting metal oxide one-dimensional nanostructures. Sensors 2009;9:9903–24.
[20] Arani MM, Niasari MS. Facile precipitation synthesis and electrochemical evaluation of Zn_2SnO_4 nanostructure as a hydrogen storage material. Int J Hydrogen Energy 2017;42:12420–9.
[21] Arani MM, Niasari MS. Novel synthesis of Zn_2GeO_4/graphene nanocomposite for enhanced electrochemical hydrogen storage performance. Int J Hydrogen Energy 2017;42:17184–91.
[22] Ashraf MA, Yang Y, Fakhri A. Synthesis of NiS–MoO_3 nanocomposites and decorated on graphene oxides for heterogeneous photocatalysis, antibacterial and antioxidant activities. Ceram Int 2020;46:8379–84.
[23] Pan H, Xie H, Chen G, Xu N, Wang M, Fakhri A. Cr_2S_3-Co_3O_4 on polyethylene glycol-chitosan nanocomposites with enhanced ultraviolet light photocatalysis activity, antibacterial and antioxidant studies. Int J Biol Macromol 2020;148:608–14.
[24] Comini E, Faglia G, Sberveglieri G. Stable and highly sensitive gas sensors based on semiconducting oxide nanobelts. Appl Phys Lett 2002;81:1869–71.
[25] Zhang G, Li C, Cheng F, Chen J. $ZnFe_2O_4$ tubes: synthesis and application to gas sensors with high sensitivity and low-energy consumption. Sensor Actuator B 2007;120:403–10.
[26] Agyemang FO, Kim H. Electrospun $ZnFe_2O_4$-based nanofiber composites with enhanced supercapacitive properties. Mater Sci Eng B 2016;211:141–8.
[27] Naseri MG, Saion EB, Kamali A. An overview on nanocrystalline $ZnFe_2O_4$, $MnFe_2O_4$, and $CoFe_2O_4$ synthesized by a thermal treatment method. ISRN Nanotech 2012;2012:1–11.
[28] Li X, Wang C, Guo H, Sun P, Liu F, Liang X, Lu G. Double-shell architectures of $ZnFe_2O_4$ nanosheets on ZnO hollow spheres for high-performance gas sensors. Appl Mater Interfaces 2015;7:17811–8.
[29] Vinoasha PA, Mely LA, Jeronsia JE, Krishnan S, Das SJ. Synthesis and properties of spinel $ZnFe_2O_4$ nanoparticles by facile co-precipitation route. Optik 2017;134:99–108.
[30] Maletin M, Moshopoulou EG, Kontos AG, Devlin E, Delimitis A, Zaspalis VT, Nalbandian L, Srdic VV. Synthesis and structural characterization of In-doped $ZnFe_2O_4$ nanoparticles. J Eur Ceram Soc 2007;27:4391–4.
[31] Chandrashekhar AL. Preparation and characterization of spinel zinc ferrite $ZnFe_2O_4$. Int J Chem Sci 2012;10:1230–4.
[32] Veith M, Haas M, Huch V. Single source precursor approach for the sol-gel synthesis of nanocrystalline $ZnFe_2O_4$ and zinc-iron oxide composites. Chem Mater 2005;17:95–101.
[33] Zhan S, Gong C, Chen D, Jiao X. Preparation of $ZnFe_2O_4$ nanofibers by sol-gel related electrospinning method. J Dispersion Sci Technol 2006;27:931–3.
[34] Zhang B, Zhang J, Chen F. Preparation and characterization of magnetic TiO_2/$ZnFe_2O_4$ photocatalysts by a sol–gel method. Res Chem Intermed 2008;34:375–80.
[35] Erdem R, Ilhan M, Ekmekci MK, Erdem O. Electrospinning, preparation and photoluminescence properties of $CoNb_2O_6$:Dy^{3+} incorporated polyamide 6 composite fibers. Appl Sci 2017;421:240–6.
[36] Ramaseshan R, Sundarrajan S, Jose R, Ramakrishna S. Nanostructured ceramics by electrospinning. J Appl Phys 2007;102.
[37] Shahabuddin M, Umar A, Tomar M, Gupta V. Custom designed metal anchored SnO_2 sensor for H_2 detection. Int J Hydrogen Energy 2017;42:4597–609.
[38] Yamazoe N. New approaches for improving semiconductor gas sensors. Sensor Actuator B 1991;5:7–19.
[39] Yamazoe N, Shimanoe K. New perspectives of gas sensor technology. Sensor Actuator B 2009;138:100–7.
[40] Hayashi Y, Yamazaki H, Masunishi K, Ikehashi T, Nakamura N, Kojima A. Effects of poisoning gases on and restoration of PdCuSi metallic glass in a capacitive MEMS hydrogen sensor. Int J Hydrogen Energy 2020;45:1187–94.
[41] Sarica N, Alev O, Arslan LC, Ozturk ZZ. Characterization and gas sensing performances of noble metals decorated CuO nanorods. Thin Solid Films 2019;685:321–8.
[42] Biswas B, Dey A, Roy S, Ray S, Sarkar SK. Pd doped TiO_2–CuO mixed metal oxide thin film sensor for H_2 sensing application. DevIC 2019:202–5. 2019–March:23–24.
[43] Lehmann S, Bauersfeld M, Wöllenstein J, Gmbh DS, Kgaa C. A copper (II) oxide–tin dioxide heterojunction sensor for the detection of hydrogen sulfide. 2018. p. 172–3.
[44] Tehrani FS, Daadmehr V, Rezakhani AT, Akbarnejad RH, Gholipour S. Structural, magnetic, and optical properties of zinc- and copper-substituted nickel ferrite nanocrystals. J Supercond Nov Magnetism 2012;25:2443–55.
[45] Liang YX, Chen YJ, Wang TH. Low-resistance gas sensors fabricated from multiwalled carbon nanotubes coated with a thin tin oxide layer. Appl Phys Lett 2004;85:666–8.
[46] Yao C, Zeng Q, Goya GF, Torres T, Liu J, Wu H, Ge M, Zeng Y, Wang Y, Jiang JZ. $ZnFe_2O_4$ nanocrystals: synthesis and magnetic properties. J Phys Chem C 2007;111:12274–8.
[47] Manohar M, Krishnamoorthi C, Naidu KCBB, Pavithra C. Dielectric, magnetic hyperthermia and photocatalytic properties of $ZnFe_2O4$ nanoparticles synthesized by solvothermal reflux method. Appl Phys A 2019;125:477–87.
[48] Tadjarodi A, Salehi M, Imani M. ZnFe2O4 nanoparticles and a clay encapsulated ZnFe2O4 nanocomposite: synthesis strategy, structural characteristics and the adsorption of dye pollutants in water. RSC Adv 2015;5:56145–56.
[49] Padil VVT, Cernik M. Green synthesis of copper oxide nanoparticles using gum karaya as a biotemplate and their antibacterial application. Int J Nanomed 2013;8:889–98.
[50] Rezvani MA, Shaterian M, Aghmasheh M. Catalytic oxidative desulphurization of gasoline using amphiphilic polyoxometalate@polymer nanocomposite as an efficient, reusable, and green organic–inorganic hybrid catalyst. Env Tech 2018;1:1–14.
[51] Rezvani MA, Asli MAN, Oveisi M, Babaei R, Qasemi K, Khandan S. An organic–inorganic hybrid based on an Anderson-type polyoxometalate immobilized on PVA as a reusable and efficient nanocatalyst for oxidative desulfurization of gasoline. RSC Adv 2016;6:53069–79.
[52] Matli PR, Zhou X, Shiyu D, Huang Q. Fabrication, characterization, and magnetic behavior of porous $ZnFe_2O_4$ hollow microspheres. Int Nano Lett 2015;5:53–9.
[53] Sancak E, Ozen MS, Erdem R, Yilmaz AC, Yuksek M, Soin T, Shah T. PA6/silver blends: investigation of mechanical and electromagnetic shielding behaviour of electrospun nanofibers. Teks ve Konfek 2018;28:229–35.
[54] Mourya S, Kumar A, Jaiswal J, Malik G, Kumar B, Chandra R. Development of Pd-Pt functionalized high performance H2 gas sensor based on silicon carbide coated porous silicon for

extreme environment applications. Sensor Actuator B Chem 2019;283:373–83.
[55] Ndaya CC, Javahiraly N, Brioude A. Recent advances in palladium nanoparticles-based hydrogen sensors for leak detection. Sensors 2019;19:4478.
[56] Zheng W, Lu X, Wang W, Li Z, Zhang H, Wang Z, et al. Assembly of Pt nanoparticles on electrospun In_2O_3 nanofibers for H_2S detection. J Colloid Interface Sci 2009;338:366–70.
[57] Park JY, Asokan K, Choi SW, Kim SS. Growth kinetics of nanograins in SnO_2 fibers and size dependent sensing properties. Sensor Actuator B 2011;152:254–60.
[58] Pan W, Ma Z, Liu J, Liu Q, Wang J. Effect of heating rate on morphology and structure of $CoFe_2O_4$ nanofibers. Mater Lett 2011;65:3269–71.
[59] Jin WX, Ma SY, Tie ZZ, Wei JJ, Luo J, Jiang XH, et al. One-step synthesis and highly gas-sensing properties of hierarchical Cu-doped SnO_2 nanoflowers. Sensor Actuator B 2015;213:171–80.
[60] Liu L, Li S, Zhuang J, Wang L, Zhang J, Li H, et al. Improved selective acetone sensing properties of Co-doped ZnO nanofibers by electrospinning. Sensor Actuator B 2011;155:782–8.
[61] Šutka A, Gross KA. Spinel ferrite oxide semiconductor gas sensors. Sensor Actuator B Chem 2016;222:95–105.
[62] Kim HJ, Lee JH. Highly sensitive and selective gas sensors using p-type oxide semiconductors: Overview. Sensor Actuator B 2014;192:607–27.
[63] Sanger A, Kumar A, Kumar A, Jaiswal J, Chandra R. A fast response/recovery of hydrophobic Pd/V_2O_5 thin films for hydrogen gas sensing. Sensor Actuator B 2016;236:16–26.
[64] Aroutiounian V. Metal oxide hydrogen, oxygen, and carbon monoxide sensors for hydrogen setups and cells. Int J Hydrogen Energy 2007;32:1145–58.
[65] Miller DR, Akbar SA, Morris PA. Nanoscale metal oxide-based heterojunctions for gas sensing: a review. Sensor Actuator B 2014;204:250–72.
[66] Seiyama T, Kagawa S. Study on a detector for gaseous components using semiconductive thin films. Anal Chem 1966;38:1069–73.
[67] Katsuki K, Fukui K. H_2 selective gas sensor based on SnO_2. Sensor Actuator B 1998;52:30–7.
[68] Korotchenkov GS, Dmitriev SV, Brynzari VI. Process development for low cost and low power consuming SnO_2 thin film gas sensors (TFGS). Sensor Actuator B 1999;54:202–9.
[69] Moon WJ, Yu JH, Choi GM. The CO and H_2 gas selectivity of CuO-doped SnO_2–ZnO composite gas sensor. Sensor Actuator B 2002;87:464–70.
[70] Han CH, Han SD, Singh I, Toupance T. Micro-bead of nanocrystalline F-doped SnO_2 as a sensitive hydrogen gas sensor. Sensor Actuator B 2005;109:264–9.
[71] Huang H, Gong H, Guo J, White TJ, Tse MS, Tan OK. Low-Temperature growth of SnO_2 nanorod arrays and tunable n–p–n sensing response of a ZnO/SnO_2 heterojunction for exclusive hydrogen sensors. Adv Funct Mater 2011;21:2680–6.